ACS APPLIED ENERGY MATERIALS

www.acsaem.org Article

Epitaxial Stabilization and Oxygen Evolution Reaction Activity of Metastable Columbite Iridium Oxide

Kyuho Lee,* Raul A. Flores, Yunzhi Liu, Bai Yang Wang, Yasuyuki Hikita, Robert Sinclair, Michal Bajdich,* and Harold Y. Hwang*

Cite This: *ACS Appl. Energy Mater.* 2021, 4, 3074−3082 Read Online

ACCESS | Metrics & More | Article Recommendations | Supporting Information

ABSTRACT: Non-rutile polymorphs of binary iridium oxide such as columbite IrO_2 (α-IrO_2) are promising candidates for highly active acid-stable oxygen evolution reaction (OER) catalysts, yet their synthesis has been challenging due to the dominant thermodynamic stability of rutile IrO_2 (R-IrO_2). Here, we report the growth of α-IrO_2 via epitaxial thin films using pulsed laser deposition. We observe that, in competition with R-IrO_2 (100), the films can be optimized to be predominantly (100)-oriented α-IrO_2. Surprisingly, the activity of α-IrO_2 shows a large discrepancy of ~0.2 V in the overpotential compared to its predicted activity, which is resolved via theoretical calculations to be a crystal orientation effect. This demonstrates that the electrocatalytic activity can be significantly varied upon crystal orientation, a parameter that is difficult to control in conventional polycrystalline systems but accessible in epitaxial thin films. In total, this study demonstrates epitaxial thin film growth as a powerful technique, which can overcome large energetic instabilities on the order of ~300 meV to stabilize metastable material structures inaccessible by bulk synthesis. This provides unique opportunities to effectively identify the atomic structure of active catalysts by combining investigations of metastable materials with theoretical predictions.

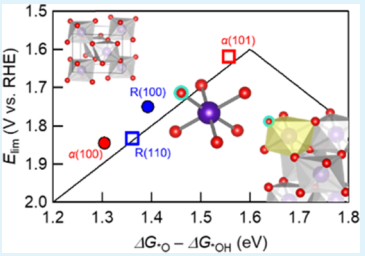

KEYWORDS: *oxygen evolution reaction, polymorph engineering, columbite iridium oxide, iridium oxide catalyst, pulsed laser deposition*

INTRODUCTION

Electricity-to-hydrogen conversion via water electrolysis is a promising energy storage mechanism for resolving the intermittency issues in renewable energy applications.[1−6] The key to enhancing the efficiency of water electrolysis lies in the catalysis of the oxygen evolution reaction (OER), the rate-limiting half-reaction of water electrolysis.[4,7] In particular, there is great interest in acid-stable OER catalysts for compatibility with polymer electrolyte membrane electrolyzers, which outperform the conventional electrolyzers in base.[8] However, the development of these catalysts remains a challenge due to the limited choice of materials which demonstrate adequate OER activity and stability in acidic and strongly oxidizing environments.[4,8,9] Consequently, a common approach has been to synthesize new structures based on the chemical composition of conventional acid-stable OER catalysts, namely iridium and ruthenium oxides.[10−13]

Recently, it was shown that strontium iridate ($SrIrO_3$) can become a highly active and acid-stable OER catalyst by selectively leaching out the A-site cations from its perovskite structure.[10] The resultant IrO_x surface structure displays an order-of-magnitude improvement in the catalytic performance in comparison with the conventional acid-stable OER catalysts, establishing this material as one of the best acid-stable OER catalysts reported thus far.[10,13] While the exact structure of this Sr-leached IrO_x active site is yet to be experimentally determined, density functional theory (DFT) calculations suggest several candidates, including different polymorphs of binary iridium oxide (IrO_2).[10]

This strongly motivates the stabilization of unconventional forms of IrO_2 via polymorph engineering, an approach that has shown great success in many oxide systems to dramatically modulate their material properties.[14−17] However, the significant thermodynamic stability of rutile IrO_2 (R-IrO_2) poses difficulties in synthesizing other non-rutile, metastable polymorphs of IrO_2.[18,19] In particular, only the pyrite phase has been observed in pressure studies of IrO_2,[18,20,21] which is in contrast with other binary oxide systems where various polymorphic transitions occur under accessible pressures.[22]

An alternate pathway may be provided by epitaxial thin film growth, in which structures that are unstable or nonexistent in bulk can nevertheless be synthesized by introducing interfacial and epitaxial strain energies.[18,23−26] Indeed, this was demonstrated in the tin dioxide (SnO_2) material system, where the metastable columbite phase was epitaxially grown using yttrium-stabilized zirconia (YSZ) as the substrate.[27−30] Although the relative instability of the columbite phase is much

Received: November 7, 2020
Accepted: March 5, 2021
Published: March 19, 2021

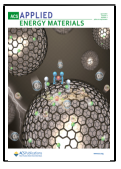

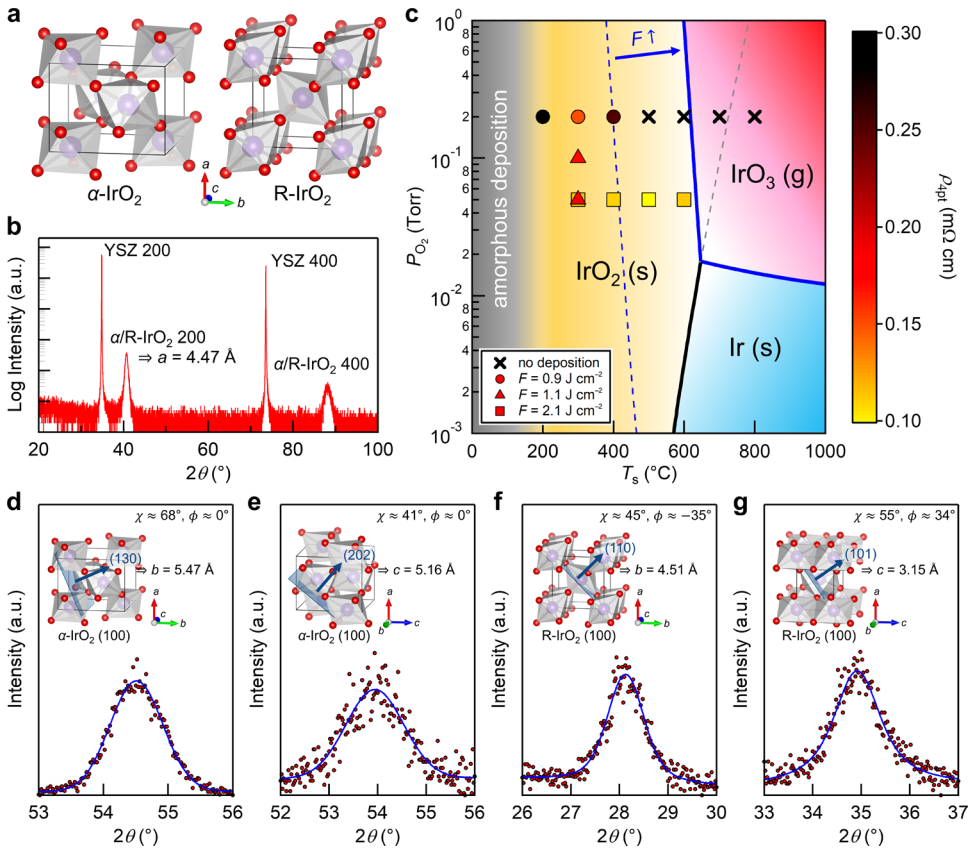

Figure 1. (a) Crystal structure of α-IrO_2 (left) and R-IrO_2 (right), with oxygen in red and iridium in purple. (b) XRD θ-2θ symmetric scan of the IrO_2/YSZ (100) film. (c) PLD growth of IrO_2/YSZ (100) (markers) overlaid by the thermodynamic calculation of the PLD growth space of IrO_x. The colors of the markers indicate the room-temperature resistivity ρ_{4pt} of the deposited films. The blue arrow indicates the shift of the IrO_2 (s)/IrO_3 (g) phase boundary as F is increased.[50] At lower fluence, the ablated materials are oxidized as IrO_3 (g), and no film deposition occurs at T_s above 400 °C due to the lowered IrO_2 (s)/IrO_3 (g) phase boundary. Increasing the fluence shifts this phase boundary to higher-temperature regions, enabling film deposition up to T_s = 600 °C. Below are the XRD θ-2θ asymmetric scans (red markers) at the (d) (130) and (e) (202) angular positions of α-IrO_2 (100) and the (f) (110) and (g) (101) angular positions of R-IrO_2 (100), with the corresponding mixed Gaussian−Lorentzian fits shown as blue solid curves.

greater for IrO_2 (the difference in the free energy of formation with the most stable phase is 3−5 kJ mol^{-1} (0.03−0.05 eV) and ∼25 kJ mol^{-1} (∼0.26 eV) for α-SnO_2 and α-IrO_2, respectively) and above the estimated stability limit of 10−20 kJ mol^{-1} in epitaxial growth,[18] this suggests an approach which we present here.

In this study, we report the epitaxial stabilization of columbite α-IrO_2 (100) on YSZ (100) using pulsed laser deposition (PLD). Careful X-ray diffraction (XRD) analysis reveals that the film is predominantly α-IrO_2 (100), with the partial formation of R-IrO_2 (100). XRD pole figures suggest a complex epitaxial relationship between the substrate and the deposited film, which is further investigated with high-resolution transmission electron microscopy (HR-TEM). The OER activity of the stabilized α-IrO_2 (100) is also measured and then compared to other relevant phases with ab initio DFT simulations to understand the origin of observed catalytic trends.

EXPERIMENTAL AND COMPUTATIONAL SECTION

Sample Preparation. IrO_2 films (∼40 nm thick) were grown by PLD using a pulsed excimer laser (KrF, λ = 248 nm) and a R-IrO_2 polycrystalline target. Samples were grown on 5 × 5 mm^2 YSZ (100) substrates, with the substrate temperature (T_s) ranging from 200 to 800 °C, oxygen partial pressure P_{O_2} ranging from 50 to 200 mTorr, laser fluence F ranging from 0.9 to 2.1 J cm^{-2}, and laser repetition rate fixed at 5 Hz. The lens was fixed at a position which maximally focuses the laser to the target. The film with the maximized volume of α-IrO_2 was obtained with T_s = 500 °C, P_{O_2} = 50 mTorr, and F = 2.1 J cm^{-2}.

Sample Characterization. XRD θ-2θ symmetric scans and reciprocal space map (RSM) measurements were conducted using a monochromated Cu $K_{\alpha 1}$ (λ = 1.5406 Å) source to identify the polymorphs formed in the films. The PANalytical X'Pert Materials Research Diffractometer equipped with Cu K_α radiation (λ = 1.5419 Å) was used for XRD pole figure measurements. Atomic force microscopy (AFM) measurements in the noncontact mode were performed to extract film surface roughness. For HR-TEM imaging, the samples were glued to form a sandwich structure (substrate/film/glue/film/substrate) and then sliced and mechanically ground to approximately 15 μm in thickness. The cross-sectional specimens were further ion-milled in a Gatan PIPS II ion milling machine to form regions with thickness below 100 nm, at which point the specimens are electron-transparent and can be viewed in TEM. Argon ion beams with 5 keV energy were induced at an incident angle of 5°, focusing at the interface between the specimens to further thin down the milled regions. For final cleaning to remove debris formed during ion milling, the beam energy was gradually reduced to 0.5 keV. HR-TEM imaging was carried out in an FEI Titan 80−300 environmental transmission electron microscope with the image corrector operating at 300 kV using negative spherical aberration imaging (NCSI) conditions. Measurements of the lattice spacing and fast Fourier transforms (FFTs) from the HR-TEM images were calibrated based on the reference lattice spacing of the YSZ substrate. The resistivity

https://doi.org/10.1021/acsaem.0c02788
ACS Appl. Energy Mater. 2021, 4, 3074−3082

measurements were conducted in a four-point geometry using Al wire-bonded contacts.

Electrochemical Measurements. The samples were cut into two 2.5 × 5 mm^2 pieces. On one of the pieces, an Ohmic back-contact was established by applying silver paste (Epoxy Technology Epo-Tek H20E) on the four edges of the film and the back of the sample. A copper wire was soldered to the back of the sample, and the entire sample-wire configuration was covered with chemically resistant epoxy (Loctite EA 9462 A Resin) except for a portion of the film with a typical area of 5 mm^2 for electrochemical measurements.[10,31] A three-electrode cell was constructed with the sample as the working electrode, Hg/Hg_2SO_4 in saturated K_2SO_4 as the reference electrode, and platinum coil as the counter electrode. The reference electrode was precalibrated against the standard hydrogen electrode. Cyclic voltammetry (CV) measurements, with each CV consisting of three potential sweeps at a rate of 10 mV s^{-1}, were repeatedly performed until steady state was reached (Figure S1). For each CV, the uncompensated resistance of the cell was obtained from electrochemical impedance spectroscopy measurements, which were taken at an open circuit from 100 kHz to 1 Hz with an AC amplitude of 10 mV. The potential values were postcorrected for 100% of the uncompensated resistance. The electrochemically active surface area (ECSA) was also monitored after each CV by measuring the double-layer capacitance, which was conducted by running potential sweeps at a 150 mV window on a non-faradic region (0.90−1.06 V vs reversible hydrogen electrode, RHE) with scan rates ranging from 5 to 100 mV s^{-1} (Figure S1).[32] Since the surface roughness R_a of the measured 60% α-IrO_2 (100) and R-IrO_2 (100) samples extracted from AFM measurements is less than 2 nm (see Figure S2), the geometrically projected surface area multiplied by the roughness factor was taken as the initial ECSA.[10,31] The Tafel plots were obtained by averaging the forward and backward scans in CV measurements. All electrochemical measurements were taken in 0.5 M H_2SO_4 under oxygen gas purge.

Computational Methods. Ab initio electronic structural simulations were performed on R-IrO_2 and α-IrO_2 using plane-wave DFT at the generalized gradient approximation (GGA) level of theory utilizing the Perdew−Burke−Ernzerhof (PBE) exchange−correlation functional[33] implemented within the Vienna ab initio simulation package (VASP).[34−36] All calculations included spin polarization and utilized the projector-augmented wave pseudopotentials[37] to represent the core electrons. A plane-wave cutoff of 500 eV and a self-consistent field (SCF) energy convergence criterium of 10^{-5} eV were used for all bulk and surface simulations. A 4 × 4 × 4 *K*-point mesh was used for bulk crystal relaxations, and a 4 × 4 × 1 *K*-point mesh was used for surface slab calculations. Ionic relaxations were performed until the maximum force component on any atom was less than 0.02 eV $Å^{-1}$. Surface slabs were cut from the bulk to model the OER mechanistic pathway and were given a minimum of 15 Å of vacuum to reduce spurious interactions between periodic images of the slabs. Dipole corrections were also applied in the *z*-direction, perpendicular to the solid surface, to counteract periodic dipoles that can occur in the slab systems. Slabs were simulated with the bottom layers fixed to bulk positions, while the top 2−4 atomic layers (depending on the polymorph) were allowed to relax. The complete set of DFT-optimized bulk and surface structures are available on Catalysis-hub.org[38] under the "LeeEpitaxial2020"[39] locator. See also Tables S1 and S2 for computed bulk properties and OER energetics.

The OER activity was modeled using the associative mechanistic pathway, which proceeds through coupled electron−proton transfers and the *OH, *O, and *OOH intermediate species.[40−43] Bader charge[44] and projected density of state (PDOS) analyses were performed on all bulk and slab structures (see Tables S3 and S4). Oxygen chemical potential-dependent surface energies were calculated on oxygen-terminated, nonstoichiometric slabs following the cell extrapolation procedure and linear fit method of Fiorentini and Methfessel[45] with an oxygen chemical potential referenced to oxygen gas at standard temperature and pressure (Figure S3).[46] Surface energies were computed from stoichiometric slabs and slabs with adsorbed oxygen to simulate oxygen-poor and oxygen-rich conditions, respectively (see Table S5).

RESULTS AND DISCUSSION

The choice of YSZ (100) ($a = b = c = 5.125$ Å) as the substrate is motivated by its large lattice mismatch with the tetragonal R-IrO_2 ($a = b = 4.51$ Å, $c = 3.16$ Å),[47] which can help suppress the stabilization of the rutile phase. Theoretical calculations on the lattice constants of α-IrO_2 ($a = 4.33$ Å, $b = 5.66$ Å, $c = 5.31$ Å) suggest that the orthorhombic α-IrO_2 (100) can have a reasonable lattice match with YSZ (100) (Figure 1a and Table S1). Given that this epitaxial environment heavily favors the stabilization of α-IrO_2 (100) over R-IrO_2, it is interesting to see whether this can help overcome the large energetic instability of ∼280 meV/IrO_2 in the columbite phase compared to that in the rutile phase and stabilize α-IrO_2 (Table S1).

Upon the optimization of the PLD growth conditions, we have obtained a film with prominent film peaks in the XRD θ-2θ symmetric scan under the growth conditions of T_s = 500 °C, P_{O_2} = 50 mTorr, and F = 2.1 J cm^{-2} (Figure 1b). The film peak positions of $2\theta \approx 40.7°$ and $2\theta \approx 88.1°$ invite several IrO_2 candidate structures,[18,19,47,48] among which are α-IrO_2 (100) and R-IrO_2 (100) (see Table S6 for the full list of the candidate structures). Ir (111) is also included as a candidate structure based on the peak positions,[49] although this is rather unlikely as the employed growth conditions are within the IrO_2 growth window according to the thermodynamic calculation of the PLD growth space of IrO_x (Figure 1c).[50]

To distinguish among these candidates, XRD θ-2θ asymmetric scans were performed at angular positions of the candidate structures. Diffraction peaks were observed at the (202) and (130) angular positions of α-IrO_2 (100) (Figure 1d,e) and the (110) and (101) angular positions of R-IrO_2 (100) (Figure 1f,g). The extracted lattice constants of α-IrO_2 ($a = 4.47$ Å, $b = 5.47$ Å, $c = 5.16$ Å) and R-IrO_2 ($a = 4.47$ Å, $b = 4.51$ Å, $c = 3.15$ Å) are in good agreement with the calculated theoretical values in this work (Table S1) as well as with the literature values,[19,47] especially considering the epitaxial strain induced by the substrate. Meanwhile, no diffraction peak was observed at the asymmetric angular positions corresponding to the other IrO_2 candidates and Ir (111). These results indicate the epitaxial stabilization of α-IrO_2 (100) together with the simultaneous growth of R-IrO_2 (100), with no other detectable phases in the film.

This columbite-rutile mixture film showed monotonic metallic behavior down to 2 K (Figure S4), with the overall resistivity value higher than the pristine R-IrO_2 (100) grown on rutile TiO_2 (100) by PLD (Figure S5). The room-temperature four-point resistivity of the mixed-phase film was measured to be 0.12 mΩ cm.

With the two IrO_2 polymorphs identified in the film, it is important to know the volume fraction as well as the relative orientation and spatial distribution of the two polymorphs to interpret the macroscopic properties of this mixed-phase film. To investigate the former, we have used the direct comparison method[51] to extract the volume fraction of the two phases from the integrated RSM diffraction peak intensity of each phase (see the Supporting Information and Figure S6). This analysis reveals that, within the explored growth conditions, the maximum α-IrO_2 (100) volume fraction of ∼60% is reached at T_s = 500 °C, P_{O_2} = 50 mTorr, and F = 2.1 J cm^{-2} (Figure 2a). This demonstrates that epitaxial films with α-IrO_2 as the

https://doi.org/10.1021/acsaem.0c02788
ACS Appl. Energy Mater. 2021, 4, 3074−3082

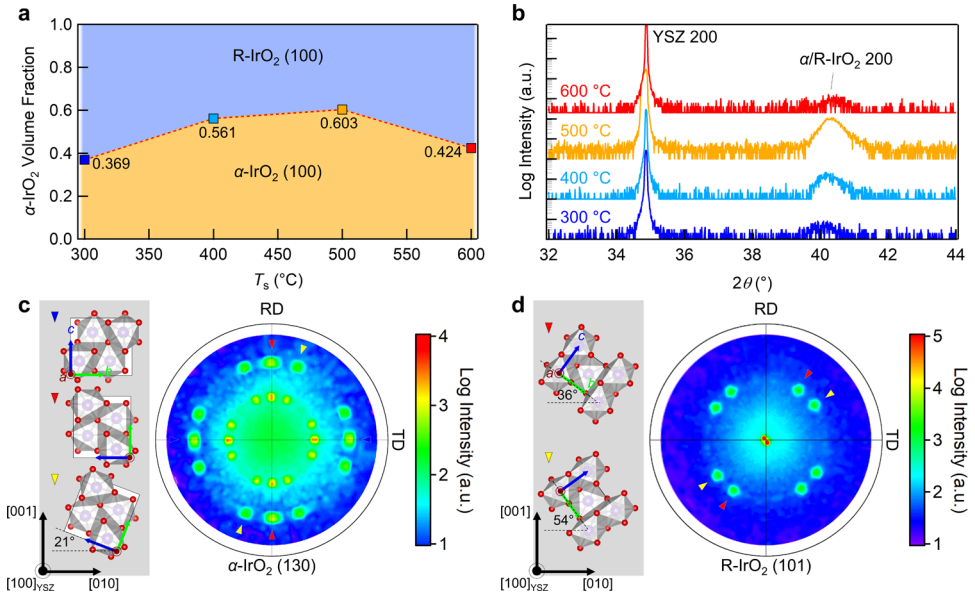

Figure 2. (a) Columbite phase volume fraction in the films grown under different T_s at P_{O_2} = 50 mTorr and F = 2.12 J cm^{-2} (square markers in Figure 1c), obtained from the direct comparison method. (b) XRD θ-2θ symmetric scans of the samples in panel (a), with T_s increasing from bottom to top. The curves are vertically offset for clarity. The reduced film peak intensity at both extremes of the explored temperature range reflects the degradation of film crystallinity. (c) XRD pole figure of α-IrO_2 (130), showing the outer set of α-IrO_2 (130) diffraction peaks and the inner set of α-IrO_2 (202) diffraction peaks. The transverse direction (TD) and the rolling direction (RD) correspond to [010] and [001] directions of YSZ, respectively. Select in-plane orientations of α-IrO_2 crystallites (triangle markers) are visualized in the left panel. (d) XRD pole figure of R-IrO_2 (101), showing the YSZ (200) diffraction peak at the center along with the outer set of R-IrO_2 (101) diffraction peaks. The TD and the RD correspond to [010] and [001] directions of YSZ, respectively. Select in-plane orientations of R-IrO_2 crystallites (triangle markers) are visualized in the left panel.

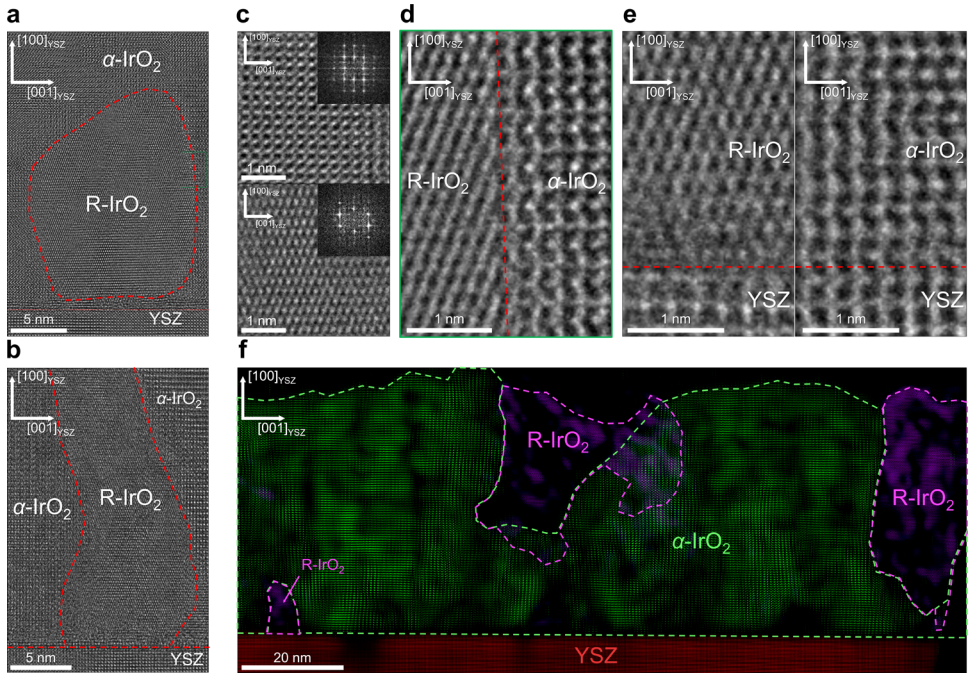

Figure 3. (a) Cross-sectional HR-TEM image of the film, showing a patch of R-IrO_2 surrounded by α-IrO_2 on top of YSZ (100). (b) Cross-sectional HR-TEM image of a different region of the film, showing a mixture of R-IrO_2 and α-IrO_2 epitaxially growing on top of YSZ (100). (c) Magnified view of α-IrO_2 (100) (top) and R-IrO_2 (100) (bottom), with the corresponding FFTs at the upper right corner. (d) Magnified view of the boundary of α-IrO_2 (100) and R-IrO_2 (100) (green box in panel (a)), showing the matching out-of-plane lattice constant of the two phases. (e) Magnified view of the substrate-film interface of R-IrO_2 (100) (left) and α-IrO_2 (100) (right). (f) Cross-sectional HR-TEM image of the film, with each crystallite distinguished via FFT filtering.

dominant phase can be synthesized. Interestingly, the α-IrO_2 (100) volume fraction correlates directly with the XRD θ-2θ film peak intensity (Figure 2b) and inversely with the in-plane film resistivity at room temperature (Figure 1c), indicating that

https://doi.org/10.1021/acsaem.0c02788
ACS Appl. Energy Mater. 2021, 4, 3074−3082

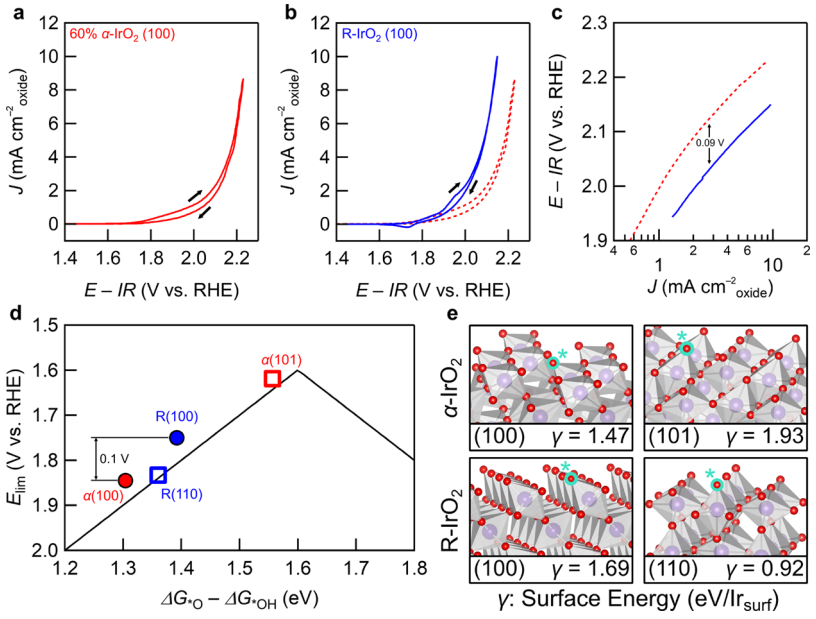

Figure 4. (a) CV measurement of 60% α-IrO_2 (100) with the normalization of the current density by the ECSA area (cm^{-2}_{oxide}). (b) CV measurement of R-IrO_2 (100) (blue solid curve) compared to (a) (red dashed curve). (c) Tafel plot of the samples in (a) (red dashed curve) and (b) (blue solid curve). The Ir redox peak region at the lower current density is truncated for R-IrO_2 (100). (d) Theoretical OER activity volcano plot of the studied columbite and rutile IrO_2 surfaces constructed from universal scaling (see Figure S9). $\alpha(hkl)$ and $R(hkl)$ refer to the (hkl) surface of columbite and rutile IrO_2, respectively. (e) Structural visualizations of the columbite and rutile surfaces with highlighted active oxygen sites. The corresponding surface energies γ of the stoichiometric slabs are also indicated (see Figure S3 for all surface energies).

the columbite phase volume fraction is maximized when the film crystallinity is maximized. In other words, the rutile phase is preferably stabilized in low-crystallinity films, which reflects the poor lattice match between R-IrO_2 (100) and YSZ (100). The degradation of film crystallinity away from T_s = 500 °C (Figure 2b) is due to the amorphous deposition limit at lower temperature and the IrO_2 (s)/IrO_3 (g) phase boundary at higher temperature (Figure 1c). As our interest is in the columbite phase, we focus on the columbite-dominant film with ~60% α-IrO_2 (100) and ~40% R-IrO_2 (100).

Next, we have investigated the epitaxial relationship of the two IrO_2 polymorphs with the YSZ (100) substrate, which is not straightforward due to the significant differences in the lattice constants and the crystal symmetry of the relevant crystallites. By taking XRD pole figure measurements on the Bragg angles of each polymorph, it is possible to individually identify the epitaxial relationships of each polymorph with the substrate. First, the XRD pole figure at the α-IrO_2 (130) Bragg angle (Figure 2c) shows two sets of peaks, the outer set corresponding to the α-IrO_2 (130) diffraction peaks and the inner set corresponding to the α-IrO_2 (202) diffraction peaks. The α-IrO_2 (202) diffraction peaks are simultaneously observed due to the similar Bragg angles of α-IrO_2 (130) and α-IrO_2 (202) ($2\theta \approx 54.29°$ and $2\theta \approx 54.26°$, respectively). The strong diffraction peaks at $\phi = 90n°$, where n is an integer, indicate the two crystal orientations of (1) $(100)_{\alpha\text{-}IrO_2}\|(100)_{YSZ}$, $[001]_{\alpha\text{-}IrO_2}\|[001]_{YSZ}$ and (2) $(100)_{\alpha\text{-}IrO_2}\|(100)_{YSZ}$, $[010]_{\alpha\text{-}IrO_2}\|[001]_{YSZ}$. Additional diffraction peaks with smaller intensity at $\phi \approx 90n \pm 21°$ indicate that a minor portion of the α-IrO_2 crystallites are distorted in-plane by ±21° from the two aforementioned orientations (Figure 2c). Meanwhile, the pole figure at the R-IrO_2 (101) Bragg angle (Figure 2d) shows R-IrO_2 (101) diffraction peaks at $\phi \approx 90n \pm 36°$, suggesting four distinct crystal orientations in total. The first two are (1) $(100)_{R\text{-}IrO_2}\|(100)_{YSZ}$, $[02\bar{1}]_{R\text{-}IrO_2}\|[001]_{YSZ}$ and (2) $(100)_{R\text{-}IrO_2}\|(100)_{YSZ}$, $[021]_{R\text{-}IrO_2}\|[001]_{YSZ}$. The remaining two orientations are obtained via 90° in-plane rotation from the first two orientations. Overall, these complex epitaxial relationships reflect the nontrivial lattice mismatch between the substrate and the two stabilized polymorphs.

To understand the spatial distribution of the two IrO_2 polymorphs, we have taken cross-sectional HR-TEM images of the film (Figures 3 and S7). These images are readily correlated with the projected respective crystal structures in the relevant zone axis directions. The images first confirm the epitaxial costabilization of α-IrO_2 and R-IrO_2 (Figure 3a–e), with α-IrO_2 being the dominant phase (Figure 3f). The matching out-of-plane lattice constant of the two phases is also observable from the cross-sectional images at the boundary between α-IrO_2 and R-IrO_2 (Figure 3d). These images indicate that the R-IrO_2 crystallites show little spatial preference throughout the film, stabilizing epitaxially on top of YSZ (100) in some cases (Figure 3b,e,f) and growing locally above α-IrO_2 while still maintaining (100) orientation in other cases (Figure 3a,d,f). This reflects the competition between the epitaxial energy and the thermodynamic stability of the two polymorphs. In terms of the epitaxial relationship with YSZ (100), α-IrO_2 (100) is heavily favored to stabilize in comparison with the poorly matched R-IrO_2, resulting in the dominant stabilization of α-IrO_2 despite its thermodynamic instability relative to the rutile form. However, there are limitations in the lattice matching between α-IrO_2(100) and YSZ (100), as the symmetry of the orthorhombic α-IrO_2 (100) lattice is different from that of the cubic YSZ (100) substrate (+6.3% mismatch on the b-lattice constant and +0.7% mismatch on the c-lattice constant). Hence, in local regions of the film where the epitaxial match of α-IrO_2(100) is

https://doi.org/10.1021/acsaem.0c02788
ACS Appl. Energy Mater. 2021, 4, 3074−3082

unsatisfied, the thermodynamically favored rutile phase is stabilized instead. This results in the costabilization of rutile and columbite phases of IrO_2.

The small lateral dimensions of the rutile crystallites (Figure 3f) and the stoichiometric equivalence of the two polymorphs make it challenging to quantitatively probe the macroscopic surface area fraction of the two phases. However, from multiple TEM images, we observe that the two phases tend to grow simultaneously in a vertical fashion throughout the film (see, for example, Figure S7a−e). In addition, the local rutile crystallites seem to stabilize across the film with no particular spatial preference (Figure 3f). Based on these observations, we approximate the surface of the film to have a similar ratio of the two polymorphs as in the bulk. Within this approximation, the electrochemical measurements on the film would imply roughly 60 and 40% contributions from α-IrO_2 (100) and R-IrO_2 (100), respectively. To compare the OER performance of α-IrO_2 (100) with that of R-IrO_2 (100), cyclic voltammetry measurements were conducted on the 60% α-IrO_2 (100) film and a pristine R-IrO_2 (100) film grown on the rutile TiO_2 (100) substrate by PLD (Figure S5). The cyclic voltammetry of the two films showed a similar profile (Figure 4a,b), with the peak around ∼1.7 V vs RHE attributed to the redox of the oxidized Ir species commonly observed in iridium oxide under similar conditions.[52,53] Interestingly, the 60% α-IrO_2 (100) film showed appreciably lower OER catalytic activity than R-IrO_2 (100). In particular, the R-IrO_2 (100) film can reach a current density of 10 mA cm^{-2}_{oxide} at 2.15 V vs RHE, while at the same potential, the 60% α-IrO_2 (100) film only outputs a current density of 3.44 mA cm^{-2}_{oxide} (Figure 4a,b). These two films show an essentially identical Tafel slope of ∼250 mV dec^{-1} in the linear region of the Tafel plot within the explored range of current density (Figure 4c), with the 60% α-IrO_2 (100) film vertically shifted up by ∼0.09 V vs RHE with respect to the R-IrO_2 (100) film due to poorer OER catalytic activity. We note that the large Tafel slope here compared to the typical reported values of 40−140 mV dec^{-1} for IrO_2 under pH 0 environment[54−56] is due to the operation under large potential bias (Figure S10).

Although the heterogeneous nature of the 60% α-IrO_2 (100) sample makes it difficult to extract the intrinsic OER activity of α-IrO_2 (100), it is evident from the higher activity of the 100% R-IrO_2 (100) sample that α-IrO_2 (100) has lower activity than R-IrO_2 (100). To understand these observations in the context of the high activity predicted for α-IrO_2 (101) in the literature,[48] we have performed theoretical calculations of the OER activity of the (100) and (101) surfaces of α-IrO_2 as well as the (100) and (110) surfaces of R-IrO_2. Figure 4d shows the calculated thermodynamic OER activity of these surfaces and their relative positions on the OER volcano plot. The volcano plot relates the predicted theoretical OER limiting potential E_{lim} (i.e. theoretical overpotential + 1.23 V thermodynamic onset potential) with the $\Delta G_{*O} - \Delta G_{*OH}$ adsorption energy descriptor, which reflects the binding strength of the catalyst surface to the reaction intermediates.[40−43] A direct comparison of E_{lim} between rutile and columbite shows that α-IrO_2 (100) has an E_{lim} of ∼0.1 eV higher than R-IrO_2 (100) (1.85 and 1.75 V vs RHE, respectively; see Figure 4d), which is in agreement with the lower activity observed for α-IrO_2 (100) (Figure 4c). We have also reproduced previous calculations on α-IrO_2 (101),[48] which shows that an ∼0.23 V higher-onset potential is expected for the (100) facet (1.62 and 1.85 V vs RHE, respectively) (Figure 4d). These results indicate that the observed low OER activity of the columbite phase is due to the difference in the (100) and (101) facets of α-IrO_2. Meanwhile, such a difference of ∼0.23 V between the onset potentials of the two columbite facets is significantly larger than that known from other reports of facet-dependent variations in the OER activity in R-IrO_2 and R-RuO_2 systems (20−50 mV).[52,57] This demonstrates that crystal orientation can play a crucial role in OER activity, shifting the onset potential of catalysts on the order of 0.1 V.

Since the active sites of both the (100) and (101) facets of α-IrO_2 are octahedrally coordinated Ir-O units, it is somewhat surprising that there is such a large activity difference between the two facets. To understand this mismatch, we have performed PDOS, Bader charge localization, and oxidation state analyses based on formal charges of O^{2-}, OH^-, and the local environment (see Table S3 and Figures S11 and S12). The charge analyses reveal that the Ir-active sites are more oxidized in the α-IrO_2 (101) facet (Table S3 and Figure S12). This is structurally reflected in the larger decrease of the surface-active site Ir-O bond length relative to the bulk for the (101) facet (Figure S13). From the PDOS calculations, we observe that the energy of the O 2*p*-band center is higher for the (101) facet (Figure S11). Based on the scaling relation between the energy of the O 2*p*-band center with ΔG_{*O} and ΔG_{*OH} (Figure S12),[58] this implies that the (101) facet has weaker reaction intermediate adsorption strength. Overall, these analyses reveal that under OER conditions, the (101) Ir-active site is more oxidized than its (100) analogue due to more oxygens singly/doubly bound to the surface Ir-active site. The higher oxidation of the active sites weakens the adsorption to the *O reaction intermediate, corresponding to the rightward shift in the OER volcano plot and resulting in higher activity (Figure 4d). Ultimately, this analysis reveals that the identification of the exposed crystal facet is crucial in determining the OER activity by way of their effect on the local coordination environments of the exposed surface sites.

Given the good agreement between the theoretical calculations and the experimental observations, we believe that α-IrO_2 (101) can be a highly active OER catalyst. To understand the relative stability of this facet, we have investigated the surface energies of the relevant facets of α-IrO_2 and R-IrO_2 discussed. Figure 4e shows the atomistic models of the simulated surfaces with highlighted singly coordinated active sites (O_{1c}) and the corresponding surface energies of stoichiometric slabs. The evolution of the surface energy from stoichiometric slabs (representing synthesis conditions) to oxidized slabs (representing OER conditions) is shown in Figure S3. We first observe R-IrO_2 (110) to be more stable than R-IrO_2 (100) under both synthesis and OER conditions, in agreement with previous studies.[59,60] For α-IrO_2, the (101) facet is less stable than the (100) facet for all chemical potentials less oxidative than the OER conditions, although this effect is less pronounced when considering surface energies normalized per surface area instead of surface units (Figure S3). This result is consistent with the larger number of Ir-O bonds broken (4 vs. 3 per surface unit) at the surface for the (101) facet compared to that for the (100) facet (Figure S14 and Table S5). Considering the additional bulk instability of the columbite phase (+0.28 eV/IrO_2 vs rutile; Table S1), this indicates that α-IrO_2 (101) is the least stable among the four investigated facets.

In awareness of the strong interest in the electrocatalysis community toward higher-activity acid-stable OER catalysts,

https://doi.org/10.1021/acsaem.0c02788
ACS Appl. Energy Mater. 2021, 4, 3074−3082

here we briefly outline the synthesis strategies of α-IrO_2 (101). As previously mentioned, there is significant thermodynamic instability of this highly active facet due to the large bulk and surface formation energies. However, the stabilization of α-IrO_2 (100) in this work demonstrates that epitaxial thin film growth can overcome large energetic instabilities, on the order of ~280 meV/IrO_2 in this particular case. Surface energy calculations also suggest that the (101) facet stability can be improved by increasing the oxygen chemical potential during synthesis (Figure S3). These observations suggest that α-IrO_2 (101) can possibly be stabilized if well-matched epitaxy is ensured. The challenge here is to find substrates compatible with the large in-plane lattice constants of this facet (6.85 and 5.66 Å). A potential solution is to tailor the substrate choice to achieve higher-order epitaxy. Using buffer layers to mitigate the epitaxial mismatch between the film and the substrate can also be a possibility.[61] We believe that theoretical investigations to search for an appropriate buffer layer to realize the epitaxial stabilization of α-IrO_2 (101) could be insightful here. Further investigations in the synthetic strategy of α-IrO_2 (101) are called for to pursue higher activity in the acid-stable IrO_2 system.

CONCLUSIONS

In summary, we have successfully synthesized α-IrO_2 (100) via costabilization with R-IrO_2 (100) in the form of epitaxial thin films. To the best of our knowledge, this is the first known stabilization of α-IrO_2. The measured lattice parameters of α-IrO_2 are a = 4.47 Å, b = 5.47 Å, and c = 5.16 Å, in good agreement with the theoretical calculations considering the epitaxial strain imposed by the YSZ substrate. XRD analysis and HR-TEM images confirmed that the growth conditions can be optimized to produce columbite-dominant films, with up to ~60% volume fraction of α-IrO_2(100). The rutile crystallites were essentially randomly distributed with no spatial preference within the film, but with robust (100) orientation to match the out-of-plane lattice constant with α-IrO_2 (100). Electrochemical measurements revealed that α-IrO_2 (100) has lower OER catalytic activity than R-IrO_2 (100), consistent with theoretical calculations. We also confirmed the literature calculations, where the (101) facet of α-IrO_2 was identified to be more active than the (100) facet.[48] We rationalize the large difference in the theoretically predicted OER activity between the two facets of α-IrO_2 to be due to significantly altered local coordination at the surface. Namely, the (101) active site has more severed bonds at the surface, which leads to more highly oxidized Ir sites with higher surface and adsorption energies. The underlying structural and electronic factors indicate that crystal orientation can significantly influence OER catalysis by changing the local coordination environment of the active sites.

The epitaxial stabilization of α-IrO_2 (100) despite the large energetic instability of ~280 meV/IrO_2 relative to the bulk stable phase is a strong demonstration that the direct verification of theoretically predicted, metastable structures for electrocatalysis can be realized via epitaxial thin film growth. In particular, the well-defined crystal orientation of these epitaxial thin films provides a unique platform for atomistic evaluation of the electrocatalytic properties, which has been limited in conventional polycrystalline systems. Overall, we believe that this method of direct synthesis and verification of theoretically predicted catalyst structures can greatly accelerate the development of high-performance electrocatalysts.

ASSOCIATED CONTENT

Supporting Information

The Supporting Information is available free of charge at https://pubs.acs.org/doi/10.1021/acsaem.0c02788.

Description of the direct comparison method, ECSA measurements and cyclic voltammetry plots, supplementary structural characterizations of the α-IrO_2 and R-IrO_2 films, and supplementary theoretical calculations and discussions of the IrO_2 activity and stability (PDF)

AUTHOR INFORMATION

Corresponding Authors

Kyuho Lee − *Department of Physics, Stanford University, Stanford, California 94305, United States; Stanford Institute for Materials & Energy Sciences, SLAC National Accelerator Laboratory, Menlo Park, California 94025, United States;* orcid.org/0000-0002-0817-0499; Email: kyuho@stanford.edu

Michal Bajdich − *SUNCAT Center for Interface Science and Catalysis, SLAC National Accelerator Laboratory, Menlo Park, California 94025, United States*; Email: bajdich@stanford.edu

Harold Y. Hwang − *Stanford Institute for Materials & Energy Sciences, SLAC National Accelerator Laboratory, Menlo Park, California 94025, United States; Geballe Laboratory for Advanced Materials, Department of Applied Physics, Stanford University, Stanford, California 94305, United States*; Email: hyhwang@stanford.edu

Authors

Raul A. Flores − *Department of Chemical Engineering, Stanford University, Stanford, California 94305, United States; SUNCAT Center for Interface Science and Catalysis, SLAC National Accelerator Laboratory, Menlo Park, California 94025, United States;* orcid.org/0000-0001-5047-2530

Yunzhi Liu − *Department of Materials Science and Engineering, Stanford University, Stanford, California 94305, United States;* orcid.org/0000-0003-0524-4023

Bai Yang Wang − *Department of Physics, Stanford University, Stanford, California 94305, United States; Stanford Institute for Materials & Energy Sciences, SLAC National Accelerator Laboratory, Menlo Park, California 94025, United States*

Yasuyuki Hikita − *Stanford Institute for Materials & Energy Sciences, SLAC National Accelerator Laboratory, Menlo Park, California 94025, United States*

Robert Sinclair − *Department of Materials Science and Engineering, Stanford University, Stanford, California 94305, United States*

Complete contact information is available at: https://pubs.acs.org/10.1021/acsaem.0c02788

Author Contributions

The manuscript was written through contributions of all authors. All authors have given approval to the final version of the manuscript.

Notes

The authors declare no competing financial interest.

https://doi.org/10.1021/acsaem.0c02788
ACS Appl. Energy Mater. 2021, 4, 3074−3082

■ ACKNOWLEDGMENTS

The authors thank A. Vailionis for discussions on XRD characterization and pole figure measurements. This work was supported by the Laboratory Directed Research and Development program at SLAC National Accelerator Laboratory (characterization); the U.S. Department of Energy Office of Basic Energy Sciences (DOE BES), Division of Materials Sciences and Engineering under Contract DE-AC02-76SF00515 (synthesis); and the DOE BES Chemical Sciences, Geosciences, and Biosciences (CSGB) Division under Contract DE-AC02-76SF00515 to the SUNCAT Center for Interface Science and Catalysis (theory). R.A.F. and M.B. acknowledge the use of the computer time allocation for the transition-metal oxide and metal surfaces: applications and reactivity trends in catalysis at the National Energy Research Scientific Computing Center, a DOE Office of Science User Facility supported by the Office of Science of the U.S. Department of Energy. Y.L. and R.S. acknowledge the financial support from the Toyota Research Institute, Accelerated Materials Design and Discovery (TRI-AMDD) program (Stanford University). Part of this work (XRD pole figure measurement and HR-TEM) was performed at the Stanford Nano Shared Facilities (SNSF) and Stanford Nanofabrication Facility (SNF) supported by the National Science Foundation under award ECCS-1542152.

■ REFERENCES

(1) Turner, J. A. Sustainable Hydrogen Production. *Science* **2004**, *305*, 972−974.
(2) Ibrahim, H.; Ilinca, A.; Perron, J. Energy Storage Systems−Characteristics and Comparisons. *Renewable Sustainable Energy Rev.* **2008**, *12*, 1221−1250.
(3) Cook, T. R.; Dogutan, D. K.; Reece, S. Y.; Surendranath, Y.; Teets, T. S.; Nocera, D. G. Solar Energy Supply and Storage for the Legacy and Nonlegacy Worlds. *Chem. Rev.* **2010**, *110*, 6474−6502.
(4) Fabbri, E.; Habereder, A.; Waltar, K.; Kötz, R.; Schmidt, T. J. Developments and Perspectives of Oxide-Based Catalysts for the Oxygen Evolution Reaction. *Catal. Sci. Technol.* **2014**, *4*, 3800−3821.
(5) Montoya, J. H.; Seitz, L. C.; Chakthranont, P.; Vojvodic, A.; Jaramillo, T. F.; Nørskov, J. K. Materials for Solar Fuels and Chemicals. *Nat. Mater.* **2017**, *16*, 70−81.
(6) Suen, N.-T.; Hung, S.-F.; Quan, Q.; Zhang, N.; Xu, Y.-J.; Chen, H. M. Electrocatalysis for the Oxygen Evolution Reaction: Recent Development and Future Perspectives. *Chem. Soc. Rev.* **2017**, *46*, 337−365.
(7) Seh, Z. W.; Kibsgaard, J.; Dickens, C. F.; Chorkendorff, I.; Nørskov, J. K.; Jaramillo, T. F. Combining Theory and Experiment in Electrocatalysis: Insights into Materials Design. *Science* **2017**, *355*, No. eaad4998.
(8) Carmo, M.; Fritz, D. L.; Mergel, J.; Stolten, D. A Comprehensive Review on PEM Water Electrolysis. *Int. J. Hydrogen Energy* **2013**, *38*, 4901−4934.
(9) McCrory, C. C. L.; Jung, S.; Peters, J. C.; Jaramillo, T. F. Benchmarking Heterogeneous Electrocatalysts for the Oxygen Evolution Reaction. *J. Am. Chem. Soc.* **2013**, *135*, 16977−16987.
(10) Seitz, L. C.; Dickens, C. F.; Nishio, K.; Hikita, Y.; Montoya, J.; Doyle, A.; Kirk, C.; Vojvodic, A.; Hwang, H. Y.; Norskov, J. K. A Highly Active and Stable $IrO_x/SrIrO_3$ Catalyst for the Oxygen Evolution Reaction. *Science* **2016**, *353*, 1011−1014.
(11) Lebedev, D.; Povia, M.; Waltar, K.; Abdala, P. M.; Castelli, I. E.; Fabbri, E.; Blanco, M. V.; Fedorov, A.; Coperet, C.; Marzari, N. Highly Active and Stable Iridium Pyrochlores for Oxygen Evolution Reaction. *Chem. Mater.* **2017**, *29*, 5182−5191.
(12) Wu, Y.; Sun, W.; Zhou, Z.; Zaman, W. Q.; Tariq, M.; Cao, L.; Yang, J. Highly Efficient Oxygen Evolution Activity of Ca_2IrO_4 in an Acidic Environment due to Its Crystal Configuration. *ACS Omega* **2018**, *3*, 2902−2908.
(13) Miao, X.; Zhang, L.; Wu, L.; Hu, Z.; Shi, L.; Zhou, S. Quadruple Perovskite Ruthenate as a Highly Efficient Catalyst for Acidic Water Oxidation. *Nat. Commun.* **2019**, *10*, No. 3809.
(14) Sclafani, A.; Herrmann, J. M. Comparison of the Photoelectronic and Photocatalytic Activities of Various Anatase and Rutile Forms of Titania in Pure Liquid Organic Phases and in Aqueous Solutions. *J. Phys. Chem. A* **1996**, *100*, 13655−13661.
(15) Haines, J.; Léger, J. M.; Schulte, O. $Pa\bar{3}$ Modified Fluorite-Type Structures in Metal Dioxides at High Pressure. *Science* **1996**, *271*, No. 629.
(16) Sakurai, S.; Namai, A.; Hashimoto, K.; Ohkoshi, S.-I. First Observation of Phase Transformation of All Four Fe_2O_3 Phases ($\gamma \rightarrow \varepsilon \rightarrow \beta \rightarrow \alpha$-Phase). *J. Am. Chem. Soc.* **2009**, *131*, 18299−18303.
(17) Liu, H.; Wang, Y.; Wang, K.; Hosono, E.; Zhou, H. Design and Synthesis of a Novel Nanothorn VO_2(B) Hollow Microsphere and Their Application in Lithium-Ion Batteries. *J. Mater. Chem.* **2009**, *19*, 2835−2840.
(18) Mehta, P.; Salvador, P. A.; Kitchin, J. R. Identifying Potential BO_2 Oxide Polymorphs for Epitaxial Growth Candidates. *ACS Appl. Mater. Interfaces* **2014**, *6*, 3630−3639.
(19) Sen, F. G.; Kinaci, A.; Narayanan, B.; Gray, S. K.; Davis, M. J.; Sankaranarayanan, S. K. R. S.; Chan, M. K. Y. Towards Accurate Prediction of Catalytic Activity in IrO_2 Nanoclusters via First Principles-Based Variable Charge Force Field. *J. Mater. Chem. A* **2015**, *3*, 18970−18982.
(20) Ono, S.; Kikegawa, T.; Ohishi, Y. High-Pressure and High-Temperature Synthesis of a Cubic IrO_2 Polymorph. *Phys. B* **2005**, *363*, 140−145.
(21) Ono, S.; Brodholt, J. P.; Price, G. D. Structural Phase Transitions in IrO_2 at High Pressures. *J. Phys.: Condens. Matter* **2008**, *20*, No. 045202.
(22) Manjón, F. J.; Errandonea, D. Pressure-Induced Structural Phase Transitions in Materials and Earth Sciences. *Phys. Status Solidi B* **2009**, *246*, 9−31.
(23) Prinz, G. A. Stabilization of bcc Co via Epitaxial Growth on GaAs. *Phys. Rev. Lett.* **1985**, *43*, 1051−1054.
(24) Gorbenko, O. Y.; Samoilenkov, S. V.; Graboy, I. E.; Kaul, A. R. Epitaxial Stabilization of Oxides in Thin Films. *Chem. Mater.* **2002**, *14*, 4026−4043.
(25) Posadas, A.; Yau, J.-B.; Ahn, C. H.; Han, J.; Gariglio, S.; Johnston, K.; Rabe, K. M.; Neaton, J. B. Epitaxial Growth of Multiferroic $YMnO_3$ on GaN. *Appl. Phys. Lett* **2005**, *87*, No. 171915.
(26) Liu, J. Z.; Zunger, A. Thermodynamic Theory of Epitaxial Alloys: First-Principles Mixed-Basis Cluster Expansion of (In, Ga)N Alloy Film. *J. Phys.: Condens. Matter* **2009**, *21*, No. 295402.
(27) Kong, L.; Ma, J.; Zhu, Z.; Luan, C.; Ji, F. Structural, Electrical and Optical Properties of SnO_2 Films Deposited on Y-Stabilized ZrO_2(100) Substrates by MOCVD. *J. Cryst. Growth* **2010**, *312*, 2931−2935.
(28) Kong, L.; Ma, J.; Zhu, Z.; Luan, C.; Yu, X.; Yu, Q. Synthesis of Orthorhombic Structure Epitaxial Tin Oxide Film. *Mater. Lett.* **2010**, *64*, 1350−1353.
(29) Kim, S.; Kim, D.-H.; Hong, S.-H. Epitaxial Growth of Orthorhombic SnO_2 Films on Various YSZ Substrates by Plasma Enhanced Atomic Layer Deposition. *J. Cryst. Growth* **2012**, *348*, 15−19.
(30) Kan, D.; Niwa, Y.; Koganezawa, T.; Shimakawa, Y. Growth-Temperature-Dependent Coalescence Determines Structural Phase of Mist-Chemical-Vapor-Deposition-Grown SnO_2 Thin Films. *J. Appl. Phys.* **2018**, *124*, No. 125303.
(31) Lee, K.; Osada, M.; Hwang, H. Y.; Hikita, Y. Oxygen Evolution Reaction Activity in $IrO_x/SrIrO_3$ Catalysts: Correlations between Structural Parameters and the Catalytic Activity. *J. Phys. Chem. Lett.* **2019**, *10*, 1516−1522.
(32) Trasatti, S.; Petrii, O. A. Real surface area measurements in electrochemistry. *J. Electroanal. Chem.* **1992**, *327*, 353−376.

https://doi.org/10.1021/acsaem.0c02788
ACS Appl. Energy Mater. 2021, 4, 3074−3082

(33) Perdew, J. P.; Burke, K.; Ernzerhof, M. Generalized Gradient Approximation Made Simple. *Phys. Rev. Lett.* **1996**, *77*, No. 3865.
(34) Kresse, G.; Furthmüller, J. Efficiency of *Ab-Initio* Total Energy Calculations for Metals and Semiconductors Using a Plane-Wave Basis Set. *Comput. Mater. Sci.* **1996**, *6*, 15−50.
(35) Kresse, G.; Furthmüller, J. Efficient Iterative Schemes for *Ab Initio* Total-Energy Calculations using a Plane-Wave Basis Set. *Phys. Rev. B* **1996**, *54*, No. 11169.
(36) Kresse, G.; Hafner, J. *Ab Initio* Molecular Dynamics for Liquid Metals. *Phys. Rev. B* **1993**, *47*, No. 558.
(37) Blöchl, P. E. Projector Augmented-Wave Method. *Phys. Rev. B* **1994**, *50*, No. 17953.
(38) Winther, K. T.; Hoffmann, M. J.; Boes, J. R.; Mamun, O.; Bajdich, M.; Bligaard, T. Catalysis-Hub.org, an Open Electronic Structure Database for Surface Reactions. *Sci. Data* **2019**, *6*, No. 75.
(39) Computational Data, 2020. https://www.catalysis-hub.org/publications/LeeEpitaxial2020.
(40) Man, I. C.; Su, H. Y.; Calle-Vallejo, F.; Hansen, H. A.; Martinez, J. I.; Inoglu, N. G.; Kitchin, J.; Jaramillo, T. F.; Nørskov, J. K.; Rossmeisl, J. Universality in Oxygen Evolution Electrocatalysis on Oxide Surfaces. *Chem. Cat. Chem.* **2011**, *3*, 1159−1165.
(41) Friebel, D.; Louie, M. W.; Bajdich, M.; Sanwald, K. E.; Cai, Y.; Wise, A. M.; Cheng, M.-J.; Sokaras, D.; Weng, T.-C.; Alonso-Mori, R.; Davis, R. C.; Bargar, J. R.; Nørskov, J. K.; Nilsson, A.; Bell, A. T. Identification of Highly Active Fe Sites in (Ni,Fe)OOH for Electrocatalytic Water Splitting. *J. Am. Chem. Soc.* **2015**, *137*, 1305−1313.
(42) Lu, Z.; Chen, G.; Li, Y.; Wang, H.; Xie, J.; Liao, L.; Liu, C.; Liu, Y.; Wu, T.; Li, Y.; Luntz, A. C.; Bajdich, M.; Cui, Y. Identifying the Active Surfaces of Electrochemically Tuned $LiCoO_2$ for Oxygen Evolution Reaction. *J. Am. Chem. Soc.* **2017**, *139*, 6270−6276.
(43) Strickler, A. L.; Flores, R. A.; King, L. A.; Nørskov, J. K.; Bajdich, M.; Jaramillo, T. F. Systematic Investigation of Iridium-Based Bimetallic Thin Film Catalysts for the Oxygen Evolution Reaction in Acidic Media. *ACS Appl. Mater. Interfaces* **2019**, *11*, No. 34059.
(44) Henkelman, G.; Arnaldsson, A.; Jónsson, H. A Fast and Robust Algorithm for Bader Decomposition of Charge Density. *Comput. Mater. Sci.* **2006**, *36*, 354−360.
(45) Fiorentini, V.; Methfessel, M. Extracting Convergent Surface Energies from Slab Calculations. *J. Phys.: Condens. Matter* **1996**, *8*, No. 6525.
(46) Kitchin, J. R.; Reuter, K.; Scheffler, M. Alloy Surface Segregation in Reactive Environments: First-Principles Atomistic Thermodynamics Study of $Ag_3Pd(111)$ in Oxygen Atmospheres. *Phys. Rev. B* **2008**, *77*, No. 075437.
(47) Bolzan, A. A.; Fong, C.; Kennedy, B. J.; Howard, C. J. Structural Studies of Rutile-Type Metal Dioxides. *Acta Crystallogr., Sect. B: Struct. Sci.* **1997**, *53*, 373−380.
(48) Xu, Z.; Kitchin, J. R. Tuning Oxide Activity Through Modification of the Crystal and Electronic Structure: From Strain to Potential Polymorphs. *Phys. Chem. Chem. Phys.* **2015**, *17*, 28943−28949.
(49) Krikorian, N. H. The Reaction of Selected Lanthanide Carbides with Platinum and Iridium. *J. Less Common Met.* **1971**, *23*, 271−279.
(50) Nishio, K.; Hwang, H. Y.; Hikita, Y. Thermodynamic Guiding Principles in Selective Synthesis of Strontium Iridate Ruddlesden-Popper Epitaxial Films. *APL Mater.* **2016**, *4*, No. 036102.
(51) Cullity, B. D.; Stock, S. R. *Elements of X-ray Diffraction*, 3th ed.; Pearson Education Limited: United States of America, 2014.
(52) Stoerzinger, K. A.; Qiao, L.; Biegalski, M. D.; Shao-Horn, Y. Orientation-Dependent Oxygen Evolution Activities of Rutile IrO_2 and RuO_2. *J. Phys. Chem. Lett.* **2014**, *5*, 1636−1641.
(53) Kuo, D.-Y.; Kawasaki, J. K.; Nelson, J. N.; Kloppenburg, J.; Hautier, G.; Shen, K. M.; Schlom, D. G.; Suntivich, J. Influence of Surface Adsorption on the Oxygen Evolution Reaction on $IrO_2(110)$. *J. Am. Chem. Soc.* **2017**, *139*, 3473−3479.
(54) De Pauli, C. P.; Trasatti, S. Composite Materials for Electrocatalysis of O2 Evolution: IrO_2+ SnO_2 in Acid Solution. *J. Electroanal. Chem.* **2002**, *538*, 145−151.
(55) Ouattara, L.; Fierro, S.; Frey, O.; Koudelka, M.; Comninellis, C. Electrochemical Comparison of IrO_2 Prepared by Anodic Oxidation of Pure Iridium and IrO_2 Prepared by Thermal Decomposition of H_2IrCl_6 Precursor Solution. *J. Appl. Electrochem.* **2009**, *39*, 1361−1367.
(56) Fierro, S.; Kapałka, A.; Comninellis, C. Electrochemical Comparison Between IrO_2 Prepared by Thermal Treatment of Iridium Metal and IrO_2 Prepared by Thermal Decomposition of H_2IrCl_6 Solution. *Electrochem. Commun.* **2010**, *12*, 172−174.
(57) Stoerzinger, K. A.; Diaz-Morales, O.; Kolb, M.; Rao, R. R.; Frydendal, R.; Qiao, L.; Wang, X. R.; Halck, N. B.; Rossmeisl, J.; Hansen, H. A.; Vegge, T.; Stephens, I. E. L.; Koper, M. T. M.; Shao-Horn, Y. Orientation-Dependent Oxygen Evolution on RuO_2 Without Lattice Exchange. *ACS Energy Lett.* **2017**, *2*, 876−881.
(58) Dickens, C. F.; Montoya, J. H.; Kulkarni, A. R.; Bajdich, M.; Nørskov, J. K. An Electronic Structure Descriptor for Oxygen Reactivity at Metal and Metal-Oxide Surfaces. *Surf. Sci.* **2019**, *681*, 122−129.
(59) Matz, O.; Calatayud, M. Periodic DFT Study of Rutile IrO_2: Surface Reactivity and Catechol Adsorption. *J. Phys. Chem. C* **2017**, *121*, 13135−13143.
(60) Nattino, F.; Marzari, N. Operando XANES from First-Principles and its Application to Iridium Oxide. *Phys. Chem. Chem. Phys.* **2020**, *22*, 10807−10818.
(61) Lu, D.; Baek, D. J.; Hong, S. S.; Kourkoutis, L. F.; Hikita, Y.; Hwang, H. Y. Synthesis of Freestanding Single-Crystal Perovskite Films and Heterostructures by Etching of Sacrificial Water-Soluble Layers. *Nat. Mater.* **2016**, *15*, 1255−1260.

https://doi.org/10.1021/acsaem.0c02788
ACS Appl. Energy Mater. 2021, 4, 3074−3082